

Chapter 2

Basic Transducer Interfacing Concepts

Abstract Before developing reasonable interfacing and power conditioning concepts, the nature of electromagnetic vibration transducers needs to be explored. Therefore, this Chapter starts with introducing general terms of transducer interface operation and the power processing chain in Sect. 2.1. There, also a further overview of a power processing and conditioning chain is given and basic evaluation metrics are defined. Thereafter, the electromagnetic vibration transducer is studied in Sect. 2.2. Application of continuous power extraction versus averaged (buffered) power extraction is compared and optimal load ratios for fractional-voltage tracking are found. These findings are the basis for developing a MPPT approach in Sect. 2.3. The focus of the developed MPPT scheme is a trade-off between a high power extraction efficiency and low operational losses in the interface. In addition, basic rules for finding system parameter values for a given transducer specification complete this part. Then, Sect. 2.4 presents architectures, topologies, and related implementation constraints for realizing the key components of the energy-harvesting based supply layer, i.e. the rectifier, the MPPT interface, and the voltage regulation. A final summary in Sect. 2.5 concludes the main findings necessary for the transistor-level circuit development given in the following chapters.

2.1 Harvesting and Power Processing Chain

This section introduces the basic and typical configuration of an energy harvesting power processing chain. Typical operation characteristics are discussed as needed for the explanations in the chapters later on. Moreover, important electric parameters are introduced. Finally, efficiencies and evaluation metrics are defined which are necessary for performance operation.

2.1.1 Two-Stage Power Management Approach

Application Power Cycle In typical real world applications and scenarios, the ambient excitation of the transducer is neither constant nor continuous [1]. It has rather a random, and intermittent nature, and has often a wide frequency band (Sect. 1.2). This finding, in conjunction with the very low duty cycle of typical WSN operation, have been the main reasons for fundamental modification of the supply layer (Fig. 1.4).

Two-Stage Power Processing Chain In accordance to the supply layer in Fig. 1.1, namely the MPPT interface, a two-stage approach is reasonable in which a first converter extracts the most available power out of the harvester and transfers it into a energy buffer device, as shown in Fig. 2.1. This arrangement is similar to the basic principal used in power electronics for modeling loss-free rectifiers [2, p. 665].

As the MPPT interface controls its input for optimal loading the transducer, its output voltage can not be controlled, because this would require a second degree of freedom available at the MPPT converter. Instead, the voltage at buffer V_{buf} is a result of the balance between the actually available harvested energy and the required power consumption of the application.

Hence, a change of buffer energy E_{buf} is related to the balance between the generator output power and the power recently consumed by the application averaged over an application cycle:

$$\frac{E_{\text{buf}}(t)}{T_{\text{app,cycle}}} = \frac{E_g(t) - E_{\text{app}}(t)}{T_{\text{app,cycle}}}. \quad (2.1)$$

In accordance, as the buffer's energy fluctuates within an application cycle $T_{\text{app,cycle}}$, its voltage V_{buf} approaches either a minimum or a maximum value, $V_{\text{buf,min}}$ or $V_{\text{buf,max}}$, respectively. Both need to be considered as the operational and technical limits a CMOS circuit allows.

Further on, a second voltage converter is necessary as a supply voltage regulator for the application. This second converter needs high efficiency at all different application load levels, and has to deal with a fluctuant buffer voltage at its input, too.

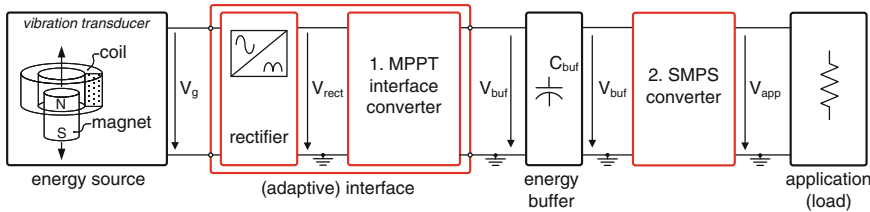


Fig. 2.1 An input-load adapting interface transfers the harvested energy on a buffer, a voltage converter provides stable and controlled output voltage to a application

2.1.2 General Interface Terms

Before dealing with a complex and real application load profile and fluctuant generator voltage amplitudes, this part assumes a sinusoidal transducer output voltages V_g . This is for defining the basic terms, which are used at many explanations and discussions later. Therefore, the generator is considered as a non-ideal AC source, thus, given with a resistive transducer model (RTM) as the schematic shows in Fig. 2.2a. This simplification is assumed as valid due to the fact that the considered real electromagnetic transducers have a large source resistance and only a very small reactance X_g (below 10 %) due to its low frequency. The applied loads are either linear (Fig. 2.2b) or, due to a rectifier and blocking capacitor, non-linear (Fig. 2.2c).

Linear Load In case of the linear load, the output terminals of the generator provides an output voltage $V_g(t)$, which is proportional to the actual open-circuit voltage $V_{g,oc}(t)$. In case of a sinusoidal excitation and zero load capacitance the generator's voltage waveform is

$$V_{g,oc}(t) = \hat{V}_{g,oc} \sin(2\pi f_g t), \quad (2.2)$$

where $\hat{V}_{g,oc}$ is the open-circuit voltage amplitude of the resistive transducer model.

As commonly known, real sources with a negligible reactance have a ratio ε_{opt} that equals both, the quotient of $V_{g,oc}$ and V_g , and the quotient between the real source impedance R_g and the real load impedance R_L . Moreover, when the real value of both (real) impedances are exactly equal, V_g is the half of $V_{g,oc}$ and the power dissipated at R_L is a maximum as given by

$$P_{g,max} = \frac{\hat{V}_{g,oc}^2}{8 R_g}. \quad (2.3)$$

However, as this optimal open-circuit voltage fraction ε_{opt} becomes different from 0.5 for complex sources, (2.3) can be expressed in a more general form with

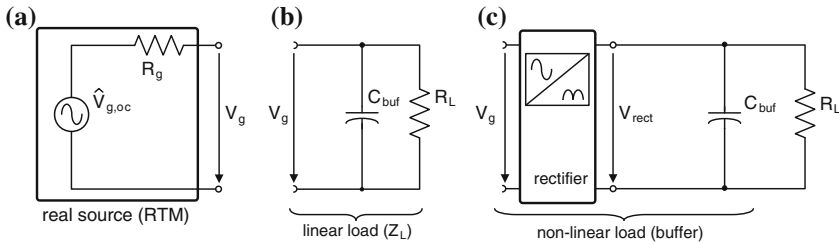


Fig. 2.2 Simplified source as a resistive transducer model (RTM) in **a** can be connected to **b** a linear load, or **c** to a rectifier with a blocking capacitor as a storage element

$$P_{g,\max} = \frac{(\hat{V}_{g,\text{oc}})^2}{2} \frac{\varepsilon_{\text{opt}}}{(1 + \varepsilon_{\text{opt}})^2} \frac{1}{R_{L,\text{opt}}}. \quad (2.4)$$

Hence, the ratio (fraction) ε_{opt} relates the actual open-circuit voltage to a voltage V_g necessary for achieving maximum power point harvesting:

$$V_{g,\text{mpp}}(t) = V_{g,\text{oc}}(t) / \varepsilon_{\text{opt}}. \quad (2.5)$$

Detailed discussion regarding real electromagnetic transducers follows in Sect. 2.2 on page 54, resulting in (2.21).

Non-linear Load In case of a non-linear load, like given in Fig. 2.2c by a rectifier and a blocking capacitor C_{buf} , the generator can supply an instantaneous output current i_g to the buffered load only when $V_{g,\text{oc}}(t)$ is higher than V_{buf} (Fig. 2.3b). Thus, the average extracted real power is calculated over a transducer period T_g with

$$\langle P_g \rangle = \frac{1}{T_g} \int_0^{T_g} v_g i_g dt. \quad (2.6)$$

Thus, the average output power $\langle P_g \rangle$ at non-linear loading will practically always be lower than the maximum available power $P_{g,\max}$ as introduced by (2.3).

The value of the optimum conduction angle α_{cond} is derived in Appendix B.3. In either case, when using the resistive transducer model (RTM) as a source the momentary power is calculated with

$$P_g(t) = v_g i_g = V_g \cdot \frac{V_{g,\text{oc}} - V_g}{R_g}. \quad (2.7)$$

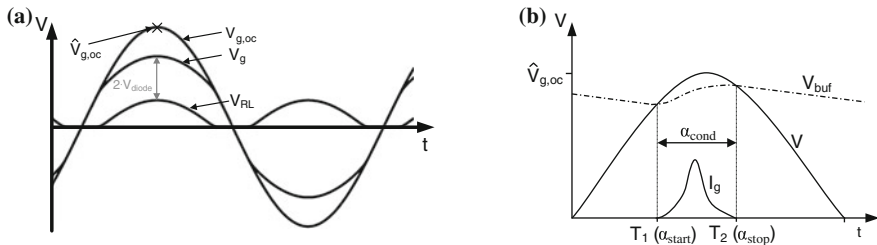


Fig. 2.3 Typical waveforms with respect to the applied load: **a** linear (resistive) load without phase shift, and **b** capacitive (non-linear) load ($C_{L,(\infty)} \gg 1/(f_g R_g)$)

2.1.3 General Efficiency Definition

Besides using a real electromagnetic generator for performance measurements, a resistive transducer is used particularly for chip characterization, too. This model is realized with a fully differential sinusoid signal generator in series with an ohmic source resistance R_g , which is typically set to $2\text{ k}\Omega$ (Fig. 2.2a). With this generator model the open-circuit voltage amplitude $\hat{V}_{g,oc}$ can be precisely set and controlled, which simplifies comparative studies at various frequencies f_g of the transducer.

Since energy harvesting is the focus two kinds of efficiencies become necessary: a power extraction efficiency, and the device efficiency. The difference of the two is the reference (denominator), which is the *maximum* available power or the *actual* available power, respectively.

Device Efficiencies Device efficiencies compare the output power to the related input power of an interface or rectifier. Therefore, as expressed by

$$\eta_{dev} = \frac{\langle P_{in} \rangle - \langle P_{L,dev} \rangle}{\langle P_{in} \rangle} = \frac{\langle P_{out} \rangle}{\langle P_{in} \rangle} \quad (2.8)$$

the real average input power to a device is compared to the output power of the same device.

While $\langle P_{in} \rangle$ is typically equal to the stepwise integrated mean output power of the transducer $\langle P_g \rangle$, the output power $\langle P_{out} \rangle$ is the actual available energy at the load element, as obtained by

$$P_{hvt} = \frac{\langle V_{buf} \rangle^2}{R_L} = \langle P_{R,L} \rangle, \quad (2.9)$$

with a small-ripple buffer voltage V_{buf} due to a large buffer capacitance C_{buf} . Thereby, the power loss $P_{L,dev}$ is the power lost within the assigned device. Hence, P_{hvt} can be actually dissipated by the real load R_L .

Power Extraction Efficiency Further on, since energy harvesting is the focus total power extraction efficiencies are defined in order to evaluate the actually harvested (extracted) power versus the maximum available power $P_{g,max}$. Therefore, the generator model is used, whose maximum power is expressed by (2.3). If the generator model is programmed for alternating amplitudes, $\hat{V}_{g,oc,1}$ and $\hat{V}_{g,oc,2}$, e.g. to study the tracking performance of an interface. then (2.3) is extended to

$$P_{g,max} = \frac{1}{2} \left(\frac{\hat{V}_{g,oc,1}^2}{8 R_g} + \frac{\hat{V}_{g,oc,2}^2}{8 R_g} \right). \quad (2.10)$$

Then, the power extraction efficiency arise given by extending (2.8) to

$$\eta_{\text{ext}} = \frac{\langle P_g \rangle}{P_{g,\text{max}}}. \quad (2.11)$$

One should note that $P_{g,\text{max}}$, as calculated with (2.3) or (2.10), is only a simplified theoretical approach. Instead, for actual evaluations with real electromagnetic vibration transducers $P_{g,\text{max}}$ is determined by reference measurements, like given by Fig. 2.9 in Sect. 2.2.

If not mentioned otherwise, all mentioned power and efficiency values are time-averaged and are obtained at settled steady-state conditions and room temperature, i.e. V_{buf} ripples around a constant DC value. The value of the used buffer capacitor C_{buf} is mentioned at the related figures.

Harvesting Efficiency In summary, the *total* harvesting efficiency η_{hvt} comprises both, the non-maximum power extraction as well as the losses of the power processing devices (η_{dev}). Thus, the harvesting efficiency η_{hvt} is defined as

$$\eta_{\text{hvt}} = \frac{\langle P_g \rangle}{\langle P_{g,\text{max}} \rangle} \cdot \eta_{\text{dev}} = \frac{\langle P_{\text{hvt}} \rangle}{\langle P_{g,\text{max}} \rangle} \quad (2.12)$$

or, if expressed with a rectifier and a voltage converter as the power processing devices the total harvesting efficiency is

$$\eta_{\text{hvt}} = \frac{\langle P_g \rangle - \langle P_{L,\text{rect}} \rangle - \langle P_{L,\text{conv}} \rangle}{P_{g,\text{max}}} = \frac{\langle P_{R,L} \rangle}{P_{g,\text{max}}}. \quad (2.13)$$

Thereby, $\langle P_{R,L} \rangle$ is the power, which can be dissipated by a load R_L connected to the storage buffer C_{buf} , i.e. as shown in Fig. 2.1 behind a MPP tracking interface device.

In summary, it can be practical to express this harvesting efficiency as a product:

$$\eta_{\text{hvt}} = \eta_{\text{ext}} \cdot \prod \eta_{\text{dev}}. \quad (2.14)$$

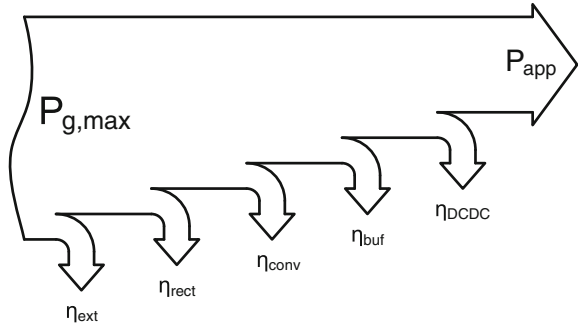
whereas η_{dev} is typically substituted by the efficiency of the rectifier (η_{rect}) and the MPPT converter. Hence, η_{hvt} compares the actually harvested and stored energy to the maximum available.

While the actual values of $P_{g,\text{max}}$ are easy and reliable to obtain, measuring the actual transducer output power P_g precisely is very difficult, particularly when the switching voltage converter interface loads the transducer. Thus, the total power extraction efficiencies η_{hvt} is often preferred in the following, since these refer to the known $P_{g,\text{max}}$.

Further Efficiencies To complete the efficiency examination along the power chain (Fig. 2.1) the converter for providing a controlled supply voltage to an application as well as the buffer introduce additional efficiency factors. All distinct efficiencies are concluded in Fig. 2.4.

One has to note that efficiencies are only defined for active states, e.g. if energy is actually harvested. However, a further important point is long-term efficiency.

Fig. 2.4 Typical energy harvesting power processing chain with all major power efficiencies



This includes especially leakage and bias current losses introduced by active circuits. This is not considered here, but it is addressed later in the designated chapters.

2.2 Interfacing of Vibrational Driven Transducers

This section introduces the considered electromagnetic harvester. In particular, the behavior is studied when linear and non-linear loads are applied. This is important for developing appropriate MPPT interface concepts.

2.2.1 Equivalent Lumped Model of Electromagnetic Vibration Transducer

The focused vibration-driven generators in this work are electromagnetic transducers. In accordance to [2–4], such transducers are modeled with an equivalent circuit representation, as shown in Fig. 2.5. Such a coupled complex transducer model is important because any electrical damping effects the mechanical behavior of the transducer due to electromechanical coupling.

2.2.1.1 Modeled Transducer Characteristics

As ambient vibrations excite an electromagnetic transducer its spring-suspended magnet moves relatively to a coil (Fig. 2.1). Such vibration-driven transducers are commonly modeled by an equivalent lumped circuit representation [2, 3], as given in Fig. 2.5. The sinusoid AC voltage source for driving the spring-mass damper system, models the mechanical force of external excitation. The coil resistance R_g , and the coil inductance L_g describe the electrical properties, and the mechanical characteristic is represented by the mass M_g , the spring compliance k_g , and the

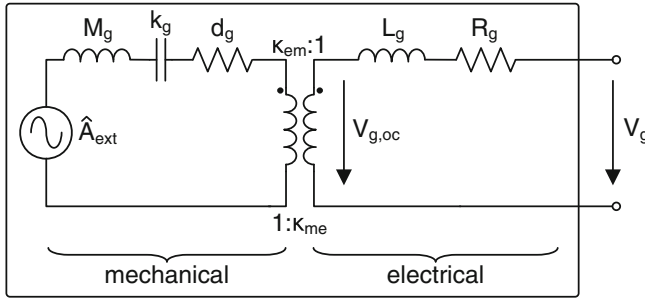


Fig. 2.5 Lumped electromechanical spring-mass-damper representation (CCTM) of an vibration-driven resonant electromagnetic energy transducer

mechanical damping coefficient d_g . Both domains are linked by a transformer with electromagnetic (EM) coupling coefficient κ [5, 6].

With typical values of the actually used electromagnetic transducers (Table B.1), four issues arise. First, there is a resonance frequency f_{res} . The values of f_{res} are calculated solely by the mechanical parameters

$$C_{eq} (68 \text{ Hz}) = \frac{1}{\omega_0^2 M_g} = 1.5 \text{ mF}. \quad (2.15)$$

This is due to the technically much larger mechanical damping effect ($d_m \gg d_e$) as reasoned in [7] (Appendix B.2).

Second, the coil resistance R_g is high, and third, it exceeds the coil reactance ($X_g = 2\pi f_{res} L_g$) significantly [8]. Hence, resistive (real) load matching instead of complex impedance matching is sufficient as also presented in Sect. 2.2.2.1.

Fourth, due to the EM coupling a force-feedback effect occurs. A dynamic change of magnetic flux ϕ_m induces a voltage $V_{g,oc}$, which is equal to the electromotive force

$$EMF = \frac{d\phi_m}{dz} \cdot \frac{dz}{dt} \quad (2.16)$$

$$= \kappa_{em} \dot{z} \quad (2.17)$$

But electric load causes an instant current i_g that is coupled back. This creates a counter force to the mechanical excitation, i.e. at constant external acceleration amplitudes (\hat{A}_{ext}) the inner elongation z is reduced. Therefore, a transformer becomes necessary in the equivalent circuit representation, which couples the electrical domain (i_g) to the mechanical domain (\dot{z}_m) by using electromagnetic coupling κ_{em} and κ_{me}

$$F_{em} = \kappa_{em} \cdot i, \quad (2.18)$$

$$F_{me} = \varepsilon = \kappa_{em} \cdot \dot{z}_m. \quad (2.19)$$

The transformer is implemented in SPICE with to complementary current-controlled voltage source (ccvs) having a gain equal to the value of the electromagnetic coupling (κ_{em} and κ_{me}).

Thus, any electrical load current reduces the transducer's amplitude. This results in an optimal load resistance $R_{L,opt}$, that is typically higher than the coil resistance R_g (Fig. 2.8 and Table B.1) [5]. As analyzed in [7, 9], $R_{L,opt}$ rather follows the relation given by (Appendix B.2)

$$R_{L,opt} = R_L + \frac{\kappa_{em}^2}{d_m}. \quad (2.20)$$

The second term describes the EM coupling effect (with transduction factor κ_{em}). Thus, any electrical load also causes a reduction of voltage $V_{g,oc}$. This actually depends weakly on the f_{res}/f_{ext} ratio, too.

The load optimum is basically obtained by setting $\partial P_{cs,max}/\partial R_L = 0$, whereas $P_{cs,max}$ is the displacement constrained maximum output power of the transducer [7] as given in Appendix B.2. The reason for taking a displacement constrained case is due to the limited mechanical amplitudes, which is technically constrained by the fixed construction volume of any transducer.

2.2.1.2 Model Verification

Measurement Setup For the measurements with the electromagnetic transducer (with the parameters given in Table B.1) a controlled vibration table is used, as shown in Fig. 2.6. This vibration table uses a closed-loop control with an acceleration sensor for keeping the amplitude of the excitation's acceleration \hat{A}_{ext} as well as the excitation frequency f_{ext} constant, so as to ensure a constant and load independent mechanical input power. Due to the resonant nature of the transducers measurements are done with setting f_{ext} equal to f_{res} .

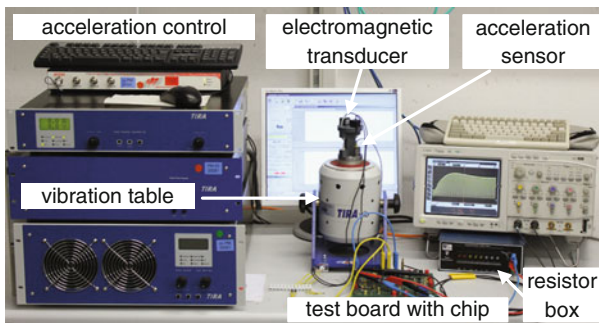


Fig. 2.6 A photography of the complete setup with controlled vibration table and transducer

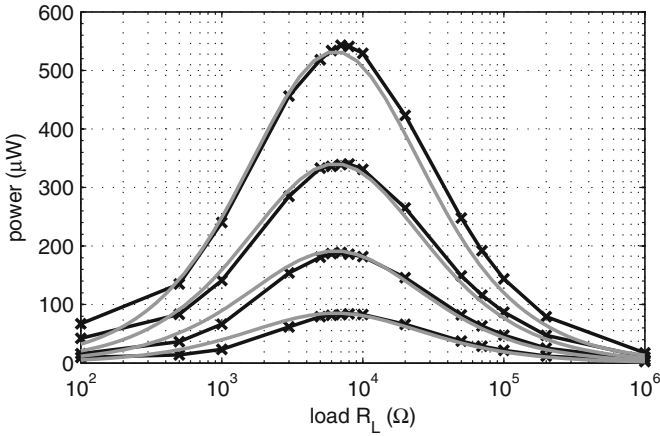


Fig. 2.7 Transducer output power P_g from measurements (*black/cross*) and simulations (*gray/solid*) with excitation amplitudes \hat{A}_{ext} of 100, 200, 300, and 400 mg ($f_{\text{ext}} = 68 \text{ Hz}$)

Comparison of Results To proof the model and the extracted values of the necessary transducer parameters (Table B.1) the plots in Fig. 2.7 show a comparison of model simulation results and measurement results. For measurement of the transducer output power at different excitation amplitudes \hat{A}_{ext} , a load resistance R_L is directly connected to the electromagnetic transducer. The same method and setup is applied for simulations with the transducer model (CCTM in Fig. 2.5). Then, $P_{g,\text{max}}$ can be calculated for each excitation level of \hat{A}_{ext} by using the root-mean square of the measured voltage across R_L . For this power calculation of the measurements sampling with 500 MS/s for DC signals, and 2 GS/s for AC signals are used. These high sampling rates are particularly useful when connecting the switching interface converters

The value of $R_{L,\text{opt}}$ matches to the simulated value by 3 % deviation. This means, if the simulated value of $R_{L,\text{opt}}$ would be applied to the real generator, its output power would be still more than 99.9 % of the measured $P_{g,\text{max}}$. Hence, using the model will give very realistic results.

The small mismatches in Fig. 2.7 can be explained by (i) weak non-linearities of the transducer vibration, e.g. κ is a weak function of the displacement amplitude [7], (ii) the magnetic loop of the transducer is not ideal, i.e. any magnetic material in the vicinity of the coil or magnet will distort the harmonic vibration, and (iii) small mismatches of the extracted values of the transducer parameters.

Altogether, the maximum achievable power with the real electromagnetic transducer is obtained by evaluation of reference measurements. Hence, as shown in Fig. 2.7 and Table 2.1, maximum power values for different excitation levels are available for serving as a reference for evaluation of the power extraction efficiencies, as introduced in Sect. 2.1.2.

Phase Shift A further issue is that any load, which is connected to the generator changes the phase shift between the excitation amplitude A_{ext} and the output voltage V_g . This becomes clear by considering that an attached load to the lumped model of Fig. 2.7 changes the impedance of the RLC network. Applying $R_{L,\text{opt}}$ as a load to the transducer specified in Table B.1, causes a phase shift in the range of 40° – 60° as compared to the open-circuit case.

2.2.2 Interfacing the Real Transducer

Practical operation of fractional voltage tracking (FVT) for MPP harvesting requires a reliable measure of the necessary $R_{L,\text{opt}}$. Only then proper adjustment of ε_{opt} is possible. Thus, it is important to have a representation of $V_{g,\text{oc}}$, which is sufficiently often updated. Therefore, the transducer model (Fig. 2.5) is tested with linear complex loads, and with non-linear loads. As it turns out, for maximizing the power extraction efficiency η_{ext} it is sufficient to neglect L_g while respecting only $R_{L,\text{opt}}$ as given by (2.20). Hence, fractional (open-circuit) voltage tracking (FVT) becomes equivalent to the adaptation of the interface input resistance to $R_{L,\text{opt}}$.

2.2.2.1 Power Extraction with Linear Loads

The values in Fig. 2.8 are normalized to $P_{g,\text{max}}$. It is obvious that using an explicit capacitive load C_{buf} for complex impedance matching is not useful to increase the harvestable power. Only very large values of C_{buf} could cause a significant drop of P_g .

Hence, the application of $R_{L,\text{opt}}$ of $6.3\text{ k}\Omega$ results in values of $P_{g,\text{max}}$ as given in Table 2.1. Thereby, the ratio of ε_{opt} as generally introduced with (2.5) is adapted to

$$\varepsilon_{\text{opt}} = \frac{\hat{V}_{g,R_{L,\text{opt}}}}{\hat{V}_{g,\text{oc},R_{L,\text{opt}}}}. \quad (2.21)$$

As expected by the linear model ε_{opt} remains constant at all values of \hat{A}_{ext} . But its usage is critical because it differs from 0.5 as it is dependent on the ratio of $f_{\text{ext}}/f_{\text{res}}$ (Fig. 2.9). However, if the ratio as given by

$$\tilde{\varepsilon}_{\text{opt}} = \frac{\hat{V}_{g,R_{L,\text{opt}}}}{\hat{V}_{g,\text{oc},R_{L=\text{inf}}}} \quad (2.22)$$

is used instead, the optimal value for $\tilde{\varepsilon}_{\text{opt}}$ is 0.5 at all values of \hat{A}_{ext} and at all values of ratio $f_{\text{ext}}/f_{\text{res}}$ (Fig. 2.9). Hence, $\tilde{\varepsilon}_{\text{opt}}$ is a reliable measure for realizing fractional voltage tracking.

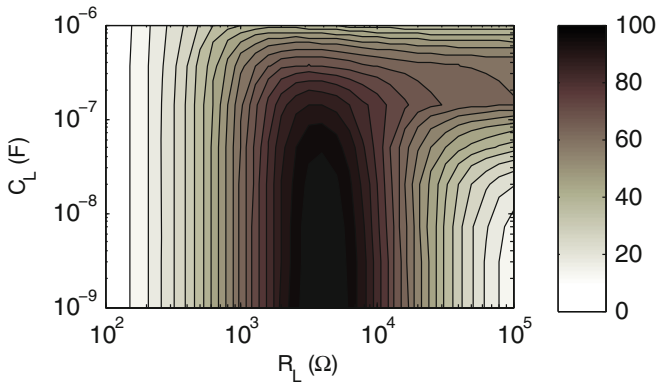


Fig. 2.8 Complex load impedance attached to the transducer model varies the output power $\langle P_g \rangle$ as R_L and $C_L = C_{\text{buf}}$ are swept

Table 2.1 Evaluation of linear loading of electromagnetic transducers with parameters of Table B.1 ($f_{\text{ext}} = 68 \text{ Hz}$)

$A_{\text{ext}}(\text{mg})$	$\hat{V}_{g, \text{oc}, R_{L=\text{inf}}}(\text{V})$	$\hat{V}_{g, \text{oc}, R_{L, \text{opt}}}(\text{V})$	$\hat{V}_{g, R_{L, \text{opt}}}(\text{V})$	$P_{g, \text{max}}^a (\mu\text{W})$	ε_{opt}	$\tilde{\varepsilon}_{\text{opt}}$
100	1.85	1.3	0.93	95	0.715	0.5
200	2.81	2.00	1.41	204	0.718	0.5
300	3.48	2.52	1.77	328	0.715	0.5

^a $R_L = R_{L, \text{opt}} = 6.3 \text{ k}\Omega$, $f_{\text{ext}} = f_{\text{res}} = 68 \text{ Hz}$

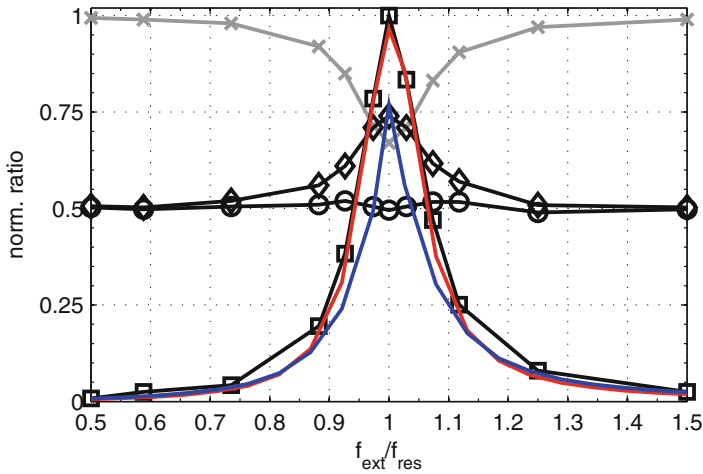


Fig. 2.9 Characteristic ratios of transducer behavior as $R_{L, \text{opt}}$ is applied, the normalized values are actually evaluated for \hat{A}_{ext} of 200 mg. ($\tilde{\varepsilon}_{\text{opt}}/\varepsilon_{\text{opt}}$ (cross), ε_{opt} (diamond), $\tilde{\varepsilon}_{\text{opt}}$ (circle), η_{ext} with $R_{L, \text{opt}}$ adapted for f_{ext} (square), η_{ext} at a fix R_L equal to $6.25 \text{ k}\Omega$ (red line)—the $R_{L, \text{opt}}$ value for f_{res} , and η_{ext} at a fix R_L of $2 \text{ k}\Omega$ (blue line)—the coil resistance

Due to the previously mentioned frequency dependency of the optimal load $R_{L,opt}$ (2.20) is valid with the given parameters in Table B.1 only for $f_{ext} = f_{res}$. In case f_{ext} differs from f_{res} the value of $R_{L,opt}$ converges to R_g , which is related to the observations available from Fig. 2.9. However, at f_{res} the value of $P_{g,max}$ obtained with R_L equal to R_g is only slightly below $P_{g,max}$ obtained with an unchanged $R_{L,opt}$ at 6.2 k Ω [10]. This is due to the resonant characteristic of the transducer.

2.2.2.2 Power Extraction with Non-linear Loads

Complementary to applying a resistive and continuous load to the transducer, using a rectifier followed by a blocking capacitor is common. Thereby, it is assumed that the blocking capacitor is sufficient for quasi-zero voltage ripple, i.e. buffer capacitance $C_{buf,\infty}$ is infinite, and the rectifier is implemented with a loss-less model. For such a non-linear load, the same concerns apply: the optimal value of the buffer voltage $V_{buf,opt}$, i.e. the optimal ratio of $V_{buf}/\hat{V}_{g,oc}$ as the dual to (2.5). Therefore, both it is important to know: the change of the generator output power as the buffer voltage is varied, and how to obtain and monitor the actual $\hat{V}_{g,oc}$.

Findings Referred to a source with a purely real internal impedance R_g , the optimal buffer voltage $V_{buf,opt}$ would be at a fraction of 0.392 of $\hat{V}_{g,oc}$ (Appendix B.3). However, as observable in Fig. 2.10, the optimal load point $V_{buf,opt}$ is shifted to higher voltages (Table 2.2). This is consistent to the previous findings with a linear load: the actual value of $\hat{V}_{g,oc}$ is a function of applied load when using the real vibration transducer or its model. For completion, the values of $\hat{V}_{g,oc, R_L=inf}$ are already listed in Table 2.1. Thereby, the optimal fraction is

$$\tilde{\epsilon}_{opt(buf)} = \frac{V_{buf,opt}}{\hat{V}_{g,oc, R_L=inf}}, \quad (2.23)$$

which yields a power ratio of

$$\tilde{\eta}_{ext,opt(buf)} = \frac{P_{g,max(buf)}}{P_{g,max(R_{L,opt})}}. \quad (2.24)$$

More interestingly, the obtained $P_{g,max(buf)}$ is also higher than the theoretical value of 0.392, as expressed by $\tilde{\eta}_{ext,opt(buf)}$. Hence, using a buffer load would (theoretically) give almost the same η_{ext} , thus, allowing a much simpler interface circuit. However, this is valid only in the case of sinusoidal waveforms. Thus, $\tilde{\epsilon}_{opt(buf)}$ is only valid for sinusoidal waveforms, too. As alternating amplitudes of \hat{A}_{ext} might appear under real world conditions, the absolute value of $V_{buf,opt}$ could not be adjusted with sufficient tracking speed due to the relative large buffer capacitance C_{buf} . Moreover, as broadband, or superimposed yet non-sinusoidal waveforms appear, the form factor will alter in addition, which certainly degrades such averaged loading additionally.

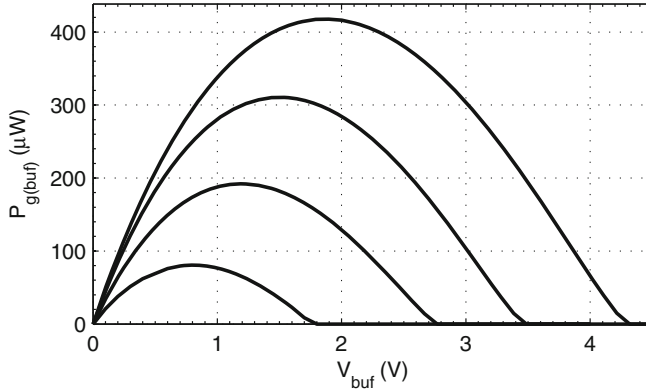


Fig. 2.10 Averaged generator power over buffer voltage V_{buf} at different generator excitation amplitudes \hat{A}_{ext} ($f_{\text{ext}} = 68 \text{ Hz}$, $A_{\text{ext}} = 100\text{--}400 \text{ mg}$)

Table 2.2 Evaluation of a buffer load on an electromagnetic transducers with parameters of Table B.1 ($f_{\text{ext}} = 68 \text{ Hz}$). $\hat{V}_{g,\text{oc}}$ and $P_{g,\text{max}}$ are for $V_{\text{buf,opt}}$ conditions

$A_{\text{ext}}(\text{mg})$	$V_{\text{buf,max}}(\text{V})$	$V_{\text{buf,opt}}(\text{V})$	$P_{g,\text{max}}(\text{buf})(\mu\text{W})$	$\tilde{\epsilon}_{\text{opt}}(\text{buf})$	$\tilde{\eta}_{\text{ext,opt}}(\text{buf})$
100	1.83	0.79	89	0.42	0.94
200	2.77	1.22	192	0.43	0.94
300	3.47	1.49	308	0.42	0.94

2.2.2.3 Main Findings on Transducer Loading

To conclude these findings, four issues dominate: first, the fact that $d_m \gg d_e$ implies that electrical compensation (by adjustment of impedance Z_L) of a mismatched f_{ext} seems impractical. Hence, active resonance tuning is not feasible with such transducers. Second, the lumped coupled transducer model is proofed as valid. The model seems sufficiently precise, while having a certain complexity. Thus, the model is considered as useful for studying and analyzing appropriate load and interfacing concepts. Third, as $X_g \ll R_g$, discontinuous power extraction methods or complex impedance matching for maximum power extraction are not useful here. An analysis in [11] states that the condition of $X_g > R_g$ is fundamental for beneficial usage of such methods. As further underpinned in [12], such a necessary reactance versus resistance relation becomes more impossible if transducers are miniaturized. Hence, since small-scale electromagnetic transducers with a low reactance are rather considered as typical, such synchronized methods are not considered throughout this book. Fourth, if non-sinusoidal waveforms shall be harvested with a highest efficiency applying a linear load for FVT seems the superior choice.

Altogether, this qualifies fractional open-circuit voltage tracking as the MPPT method of choice. The finding that there is a ratio $\tilde{\epsilon}_{\text{opt}}$ available that is independent

of excitation frequency and excitation amplitude makes realization of the fractional voltage tracking method for electromagnetic transducers possible.

2.2.3 General Load Detection Methods

As the previous Section has revealed, for achieving MPP harvesting with AC sources averaged (non-linear) as well as continuous (linear) fractional voltage tracking, AFVT and CFVT, are beneficial options (for achieving a high η_{ext}). However, in both cases the optimal load point needs to be monitored on-line when the transducer is loaded.

Thus, for both options, AFVT as well as CFVT, either an auxiliary pilot transducer is added for estimation of the actual available $V_{g,\text{oc}}(t)$, or the optimal load point needs to be derived from the loaded transducer by a detector. Hence, there are four methods of MPP harvesting using fractional voltage tracking:

AFVT Here, for the *averaged* fractional voltage tracking V_{buf} is adjusted with respect to $\hat{V}_{g,\text{oc}}$, i.e. MPP harvesting is realized with setting the buffer voltage to $V_{\text{buf,opt}}$. Regarding to the form factor of the transducer output voltage, a certain fraction $\tilde{\epsilon}_{\text{opt(buf)}}$ exists that is an optimal load, e.g. as shown previously for cases of ideal sinusoidal excitation.

- AFVT1: Sampling $\hat{V}_{g,\text{oc}}$ of an axillary pilot transducer; phase relation seems not important due to the DC tracking voltage level ($V_{\text{buf,opt}}$).
- AFVT2: Peak voltage sampling of $V_{g,\text{oc}}$ by interruption of harvesting [1], i.e. unloaded periods are necessary, which reduces η_{ext} , but a pilot transducer is avoided.

Hence, the trigger circuit for AFVT tracking could be simply a hysteretic comparator. Such a discriminator for a two-point controller has a reference voltage that is generated either by peak sampling, or by using the signal of the auxiliary transducer. While peak voltage sampling requires interruption of harvesting, using an auxiliary transducer is particularly sensible in terms of matched resonance frequencies, and mutual coupling effects, too. Both might lower the extraction efficiency η_{ext} .

CFVT Here, for the *continuous* fractional voltage tracking the voltage $V_g(t)$ is tracked with respect to the instantaneous value of $V_{g,\text{oc}}(t)$ with the optimal fraction (ϵ_{opt}). Regarding the method of determination of ϵ_{opt} two approaches are suggested:

- CFVT1: Sampling $V_{g,\text{oc}}(t)$ of an axillary generator, phase relation is important due to the direct tracking, i.e. also the auxiliary transducer needs to be loaded by $R_{L,\text{opt}}$ which is particularly important at resonant harvesting.
- CFVT2: Sampling $V_g(t)$ and I_g either with a sufficient high sampling rate during unloaded states (Chap. 6), or by a detector, which is able to identify the power-optimal load point (Chap. 7).

2.3 Dynamic Sliding Load Window MPPT

In accordance to the previous analysis, for quasi-optimal power extraction a converter is needed for continuous fractional MPP tracking. This converter needs to be able to continuously track the optimal value of V_g with respect to the programmed value of ε_{opt} . Such MPP tracking with continuous tracking is superior to alternative solution that use a blocking capacitor and adapt its optimal voltage $V_{\text{buf,opt}}$. Therefore, a general tracking concept has been invented, which is introduced in this Section. This concepts is the basis for the later load matching and continuous MPP tracking interfaces.

2.3.1 Maximum Power Point Tracking with Switch-Mode Converters

A common approach for describing a switch-mode converter as a load is using the *resistor emulation* method [2, 13]. This is typically realized with a SMPS (switch-mode power converter) for designing input-matched interfaces [2, p. 665].

MPP Tracking In general, as Fig. 2.11 suggests, a SMPS or a charge pump together with an input capacitor C_{in} allows a continuous and permanent flow of the transducer output current I_g . The SMPS is used to control the charge at C_{in} so as to continuously track the optimal V_g . Thus, such a MPPT interface converter allows AC voltage tracking for keeping V_g at a power-optimal value.

Hence, in accordance to the simple MPPT interface model of Fig. 2.11 the time-averaged input resistance $\langle R_{\text{in}} \rangle$ of the MPPT interface is defined as

$$\langle R_{\text{in}} \rangle = (1 - D) R_L = \frac{1 - T_{\text{chg}}}{T_{\text{sw}}} R_L, \quad (2.25)$$

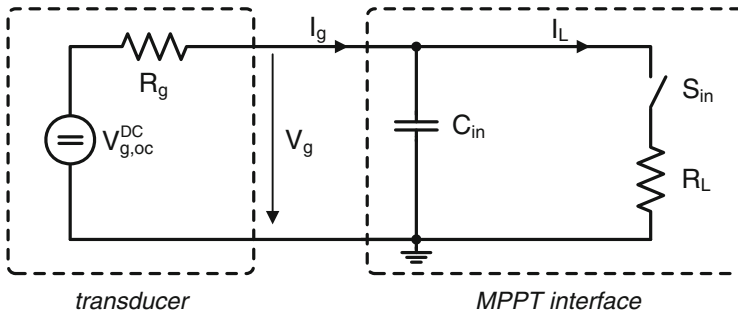


Fig. 2.11 Power extraction with a controlled switching capacitor for achieving an optimal $\langle R_{\text{in}} \rangle$

with D as the duty cycle of switch S_{in} , and T_{sw} as the time of a transfer cycles. During T_{chg} switch S_{in} is turned off while capacitor C_{in} gets charged.

Resistor emulation is possible by three different modes of operation: [2] discontinuous-conduction mode (DCM), continuous conduction mode (CCM), and boundary conduction mode (BCM). Interesting demonstrations of using the CCM and DCM approach are provided in [1] and [13], respectively.

DCM At DCM operation the coil current flow is interrupted by zero current phases. Therefore, the emulated time-averaged resistance in DCM is given a [2, p. 109]

$$R_{e,DCM} = \frac{2 L f_{sw}}{D^2}. \quad (2.26)$$

Thus, the actual input resistance $R_{e,DCM}$ can be fixed and is independent of the load. However, this is only possible if the DCM condition is given, i.e. the load current I_L is below

$$I_L < \frac{V_g}{L_{tx}} D T_{sw}. \quad (2.27)$$

CCM In CCM there is a continuous coil current flow, i.e. I_L never drops down to zero. The emulated resistance in CCM is given as

$$R_{e,CCM} = (1 - D)^2 R_L. \quad (2.28)$$

Thus, the actual input resistance $R_{e,CCM}$ can be adjusted by duty cycle D , but it also depends on the actual load R_L .

BCM This boundary mode is achieved exactly at the transition between DCM and CCM, i.e. the coil current flow is quasi-continuous, since it is zero at the end of each switch cycle. This zero-current state can be exploit for simplification of switch-mode converter control, as done in Chap. 8.

Continuous Tracking However, a switch-mode converter can only emulate an input resistance by time-averaging, i.e. during $(1 - D) T_{sw}$ no power is harvested unless an input capacitor C_{in} is used (Fig. 2.11). When using an AC source, the capacitance of C_{in} needs to be properly related to the generator parameters, f_g and R_g . If MPP tracking is assumed, then a balance between the generator voltage transients and the voltage ripple $\Delta V_{C_{in}}$ across the input capacitor can be set with

$$\frac{I_g T_{chg}}{\Delta V_{C_{in}}} \leq C_{in} \leq \frac{1}{4} \frac{1}{f_g R_g}. \quad (2.29)$$

For proper MPP tracking of AC voltages the ripple $\Delta V_{C_{in}}$ is much smaller than $V_{g,oc}$.

2.3.2 POPoC—Concept of Load Approximation

Related to the previous general introduction of Sect. 2.3.1, here, it is shown how continuous MPP tracking can be realized by using a charge pump converter.

2.3.2.1 Point of Power-Optimal Charging—POPoC

As shown in Fig. 2.12, as an empty capacitor C_{in} is charged by a non-ideal DC source, described as a purely resistive Thevenin source, the transferred power has a maximum at

$$t_{opt} = \ln(2) \cdot \tau_{chg} \Leftrightarrow P_g(t_{opt}) \rightarrow \max., \quad (2.30)$$

thereby, τ_{chg} is the time constant given by C_{in} and the source resistance R_g . At charging a capacitor, as plotted in Fig. 2.12, its voltage increases exponentially while the current decreases. This results in a power-optimal point of charging (POPoC). There, the delivered power from the source into the capacitor is maximized

$$\frac{\partial P_g}{\partial t} = \frac{\partial V_{C_{in}}(t) I_g(t)}{\partial t} = 0 \Leftrightarrow P_{g,max}. \quad (2.31)$$

Hence, as the voltage across the input capacitor C_{in} is kept close to the POPoC, harvesting is achieved at the maximum power point. At this power-optimal point of charging, the capacitor voltage is half of the actual open-circuit voltage of the source ($V_{g,oc}$). Thus, at POPoC the load exactly corresponds to the voltage condition of typical impedance matching, i.e. $V_g = 0.5 \cdot V_{g,oc}$ with a real resistive voltage source (ε_{opt} is 0.5).

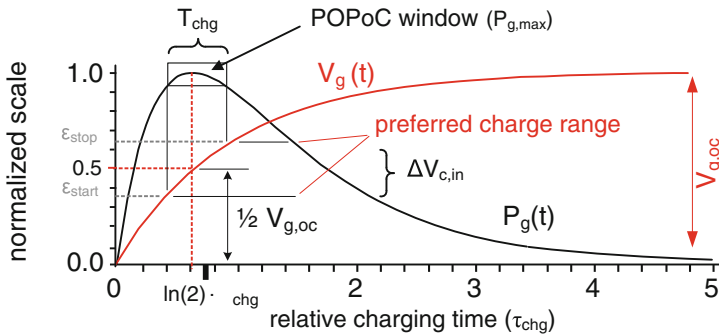


Fig. 2.12 Characteristic voltage and power transfer of a capacitor being charged. The transfer cycle is located around the power-optimal point of charging (POPoC), which needs ε_{opt} equal to 0.5 for a resistive source (RTM)

Interestingly, the value of the obtained $P_{g,\max}$ at this POPoC equals exactly the maximum power achieved by setting the ohmic load resistor R_L equal to the source resistance R_g . In addition, if the exponential equations for current and voltage are evaluated at POPoC, the equivalent resistance is

$$R_{in}(t) = \frac{V_{C_{in}}(t)}{I_g(t)} = R_g \left(\frac{1}{\exp \frac{-t}{\tau_{chg}}} - 1 \right). \quad (2.32)$$

Hence, $\langle R_{in} \rangle$ is optimal at $R_{in}(t_{opt} = \ln(2) \tau_{chg}) = R_g$. This is between a range of $R_{in,\min}$ at V_{start} , and $R_{in,\max}$ at V_{stop} , as compiled in Table 2.3. Hence, using a capacitor at the POPoC same maximum power results can be achieved as with a matching ohmic load.

POPoC Window Since the power peak (MPP), as shown in Fig. 2.12, is rather flat, a POPoC window is defined, which describes the closer vicinity around the MPP. The voltage boundaries V_{stop} and V_{start} define the actual width of the POPoC window. Using relative definitions results in

$$V_{start} = \varepsilon_{start} V_{g,oc} \quad (2.33)$$

$$V_{stop} = \varepsilon_{stop} V_{g,oc} \quad (2.34)$$

$$\varepsilon_{hyst} = \varepsilon_{stop} - \varepsilon_{start}. \quad (2.35)$$

Provided that exponential charging is given, then both voltage V_{start} and V_{stop} , can be linked to the related point in time, T_{start} and T_{stop} , respectively (Appendix C). Hence, using (2.33) and (2.34) the charging within the POPoC window needs a time of

$$T_{chg} = T_{stop} - T_{start} \quad (2.36)$$

$$= -R_g C_{in} \ln \left(\frac{1 - \varepsilon_{stop}}{1 - \varepsilon_{start}} \right). \quad (2.37)$$

This duration of T_{chg} is an important parameter for defining the necessary circuit speed.

2.3.2.2 DC Operation and Evaluation

Tracking Slots While Fig. 2.12 illustrates only a single POPoC window, Fig. 2.13 demonstrates the related continuous operation for a DC input voltage. Since $R_L \ll R_g$ the charging (T_{chg}) takes much longer than discharging (T_{dischg}) of C_{in} from V_{stop} to V_{start} . Thus, the complete cycle time T_{cycle} is very close to T_{chg} . In practice the time constant of discharging will be limited by the ESR of a further storage buffer and R_{on} of the power switch and interconnection resistances.

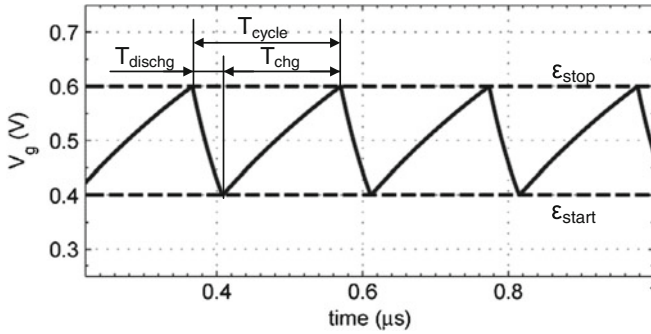


Fig. 2.13 As S_{in} is turned on and off, $\langle R_{in} \rangle$ is applied to the generator resulting in subsequent (power extraction) slots of length T_{cycle}

Table 2.3 Width of POPoC window and related power extraction efficiency η_{ext}

ε_{hyst}	η_{ext}	$T_{chg}(1/\tau_{chg})$	$\Delta V_{C_{in}}$		$R_{in,min}(t)$ ($1/R_g$)	$R_{in,max}(t)$ ($1/R_g$)
			$V_{g,oc} = 0.5$ V (mV)	$V_{g,oc} = 2.0$ V (mV)		
0.05	0.98	0.22	50	200	0.82	1.22
0.1	0.944	0.41	100	400	0.67	1.5
0.15	0.87	0.62	150	600	0.54	1.85

Extracted and Transferred Power Indeed, the extracted power equals $P_{g,max}$ only at the POPoC. However, as the actual size of the POPoC window is limited by V_{stop} and V_{start} , the extracted power, as calculated with

$$\langle P_g \rangle = \frac{1}{T_{chg}} \int_{T_{start}}^{T_{stop}} P_g dt + \frac{1}{T_{dischg}} \int_{T_{stop}}^{T_{cycle}} P_g dt, \quad (2.38)$$

is close to $P_{g,max}$ if ε_{hyst} remains small. Moreover, as the input resistor of a converter is typically rather small, and (2.38) can be simplified to

$$\langle P_g \rangle \approx \frac{1}{2} \frac{C_{in}}{T_{chg}} \left(\varepsilon_{stop}^2 - \varepsilon_{start}^2 \right) V_{g,oc}^2. \quad (2.39)$$

while assuming that $T_{chg} \approx T_{cycle}$, and $T_{dischg} \approx T_{chg}$.

This is exemplified in Table 2.3, which lists that η_{ext} will remain above 94 % if ε_{hyst} is above 10 %. Thereby, T_{start} and T_{stop} are set symmetrically around t_{opt} , as illustrated in Fig. 2.12. Hence, $\langle P_g \rangle$ calculated with (2.38) can be put into (2.11) as a nominator to calculate the values of η_{ext} in Table 2.3.

Fig. 2.14 Extraction efficiency η_{ext} with DC source voltage ($V_{g,oc} = 1 \text{ V}$, $R_g = 1 \text{ k}\Omega$) over tracking window size ($\varepsilon_{\text{hyst}}$) and position (ε_{opt}) ($C_{in} = 1 \text{ nF}$)

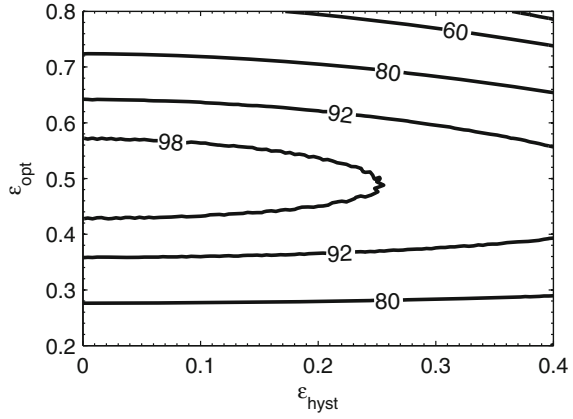
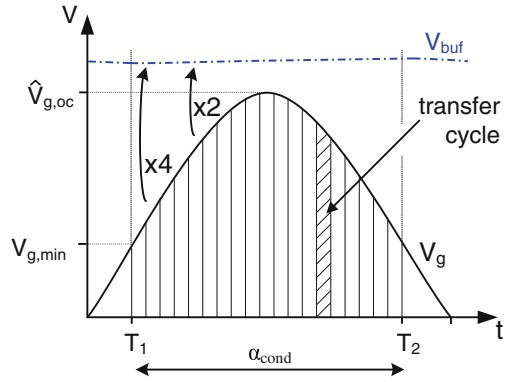


Fig. 2.15 With the adaptive interface the conduction angle α_{cond} is kept large also at high values of the buffer voltages V_{buf}



The contour plot in Fig. 2.14 approves this with results η_{ext} when the window center ε_{opt} , and the window width $\varepsilon_{\text{hyst}}$ are altered.

2.3.2.3 AC Operation and Evaluation

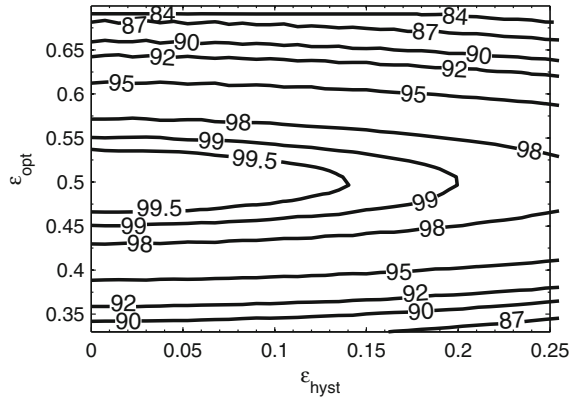
For continuous AC voltage tracking a voltage conversion ratio

$$k_V = \frac{V_{\text{buf}}}{V_g}. \quad (2.40)$$

becomes necessary. As V_{buf} remains relatively constant, this ratio k_V needs to be continuously adapted (Fig. 2.15). Then, even energy can be harvested if V_g is much lower than V_{buf} .

Provided that $T_{\text{cycle}} \ll T_g$ tracking happens in an oversampling manner, as visualized with the transfer cycles in Fig. 2.15. Thus, fractional voltage tracking of AC

Fig. 2.16 Harvesting efficiency η_{hyst} with AC source voltage ($\hat{V}_{g,oc} = 2$ V, $R_g = 1$ k Ω , $V_{g,min} = 0.5$ V) for a tracking parameter sweep ($C_{in} = 1$ nF)



sources appears like interfacing a ‘stepwise’ changing DC source. Moreover, the conduction angle α_{cond} is widened and only limited by a maximum voltage conversion ratio $k_{V,max}$ of the interface converter.

Simulation Results As seen in Fig. 2.16, continuous tracking also has a maximum at a center of ε_{opt} equal to 0.5. As long as $\varepsilon_{\text{hyst}}$ remains below 0.1 the efficiency η_{ext} is close to maximum. Hence, the extraction efficiency η_{ext} is not that sensitive to changes of the tracking window. But, due to the alternating input voltage, voltage tracking limits are introduced by the minimum and maximum voltages a converter can treat.

2.3.2.4 Operation Constraints for Continuous MPP Tracking

The input capacitance C_{in} of Fig. 2.11 has to match with the necessary AC tracking speed with respect to (2.29). For usage of oversampling slots (Fig. 2.29) in conjunction with continuous tracking, there appear additional constraints on the sizing of C_{in} . Hence, for sufficient oversampling at continuous tracking, a more detailed analysis is necessary. Therefore, the maximum change of the source voltage during a transfer cycle has to be limited to a small fraction of $V_{g,oc}$, as given by

$$\Delta V_{g,oc,max} \ll 0.1 \cdot V_{g,oc}(t). \quad (2.41)$$

Thus, to keep $\Delta V_{g,oc,max}$ small enough, a sinusoidal waveform at its maximum gradient is assumed as a worst-case situation. Then, as $\Delta V_{g,oc,max}$ is the maximum possible change of the AC source voltage during a maximum allowed transfer cycle, the related maximum cycle time is estimated with

$$T_{\text{cycle,max}} = \frac{\Delta V_{g,oc,max}}{2\pi f_g \hat{V}_{g,oc}}. \quad (2.42)$$

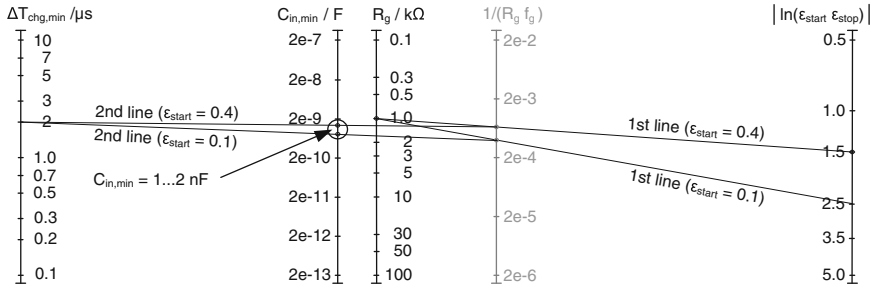


Fig. 2.17 Nomogram for determination of minimum required array capacitance $C_{in,min}$ for sufficient power transfer

Only then sufficient oversampling can be guaranteed.

Input Capacitance Range In contrast to (2.29) with (2.37) and (2.42), the input capacitance C_{in} needs to be set to the range as given with

$$\frac{t_{d,min}}{R_g \ln\left(\frac{1 - \varepsilon_{stop}}{1 - \varepsilon_{start}}\right)} \leq C_{in} \leq \frac{\min(T_{chg,max}, T_{cycle,max})}{R_g \ln\left(\frac{1 - \varepsilon_{stop}}{1 - \varepsilon_{start}}\right)} \quad (2.43)$$

Thereby, $t_{d,min}$ is the minimum switch delay, which is affordable for an appropriate low-power circuit.

Based on these rules a design table has been developed as plotted in Fig. 2.17. This nomogram allows a first estimation for matching transducer parameters, and possible circuit specifications ($t_{d,min}$, die area) with necessary tracking and matching constraints. For demonstration of this method an example shows that a R_g of 5 kΩ and f_g of 100 Hz with an amplitude of 3 V needs a $T_{chg,max}$ of 5.3 μs and a $C_{in,max}$ of 2.5 nF, which is a bearable value for on-chip implementation.

Maximum Conversion Factor and Limit of Beneficial Operation As $V_g(t)$ falls to very low values k_V increases to large values. As known for switch-mode power supplies and charge-pump converters, the conversion efficiency is typically lower for higher values of k_V [2, p. 43]. Moreover, the output power of the generator falls with its output voltage V_g . Thus, in order to keep energy harvesting with an active converter beneficial the ratio k_V needs to be limited to a reasonable $k_{V,max}$, and minimum beneficial voltage $V_{g,min}$, too.

For a first-order approach, this can be done by comparing the actual extracted average power $\langle P_g \rangle$ (as estimated by (2.39)), to the estimated device losses caused by the MPPT interface. Thus the inequality of

$$\langle P_g \rangle \cdot \eta_{hvst} \geq \sum \langle P_{L,dev} \rangle_i \quad (2.44)$$

needs to hold true, i.e. as $P_{L,dev}$ is rather fix a reasonable $V_{g,min}$ needs to be set.

2.4 Power Processing Modules

Besides efficient rectification of the AC voltages two concepts of MPP tracking with the CFVT method are introduced. Thereby, one is based on a charge-pump concept, while the second uses a switched-inductor in DCM mode. Further on, analyzing general implementation requirements and strategies are discussed, circuit specifications are addressed, and necessary innovations are considered. Moreover, in order to complete the power processing chain (Fig. 2.1) a voltage regulator concept is added.

2.4.1 Rectification

Using AC sources, like vibration driven electromagnetic transducer, the first step is rectification of the AC output voltage V_g . Therefore, before MPP tracking can happen a rectifier is required between the MPPT converter and the transducer, as already illustrated in Fig. 2.1.

A rectifier itself can not provide MPP tracking, but because of its simplicity its necessary supply power will be probably much smaller as compared to any MPPT interface. Thus, harvesting with solely a rectifier with a blocking capacitor will also serve as a reference configuration.

A particular challenge is achieving a *very wide input and supply voltage range* at which efficient rectification is possible. This is of particular interest for EH applications: even at low input amplitudes (0.5–3.3 V) sufficient load currents $I_{g,mpp}$ may cause only low voltage drops ΔV_{rect} across the conducting rectifier. Moreover, possible effects of the typical *high coil resistance* and source impedance of electromagnetic transducer⁷ need to be considered.

2.4.2 Input-Load Adapting Charge Pump—ILACP

Derived from the previously introduced POPoC concept using an adaptive charge pump converter is suggested, as illustrated in Fig. 2.18. As a high efficiency of the rectifier is assumed, i.e. a low forward voltage drop appears ($V_{rect} \approx V_g$), the switched capacitor arrays are controlled so as to comply to the POPoC window method. That is, the abstract input capacitance C_{in} of Fig. 2.11 can be implemented by two out-of-phase toggled capacitor arrays. Hence, at a time always one capacitor array can be connect to the input, while the other array is discharged onto the capacitor C_{buf} . Nevertheless, there are short switching gaps due to necessary non-overlapping toggling of the flying capacitor arrays. Thus, such gaps could be used to sample the actual open-circuit voltage $V_{g,oc}(t)$, because the transducer is unloaded during these gaps.

As an option, an additional capacitance C_{in} could harvest energy during such non-overlapping switching gaps. Hence, increasing η_{ext} . But, due to such permanent

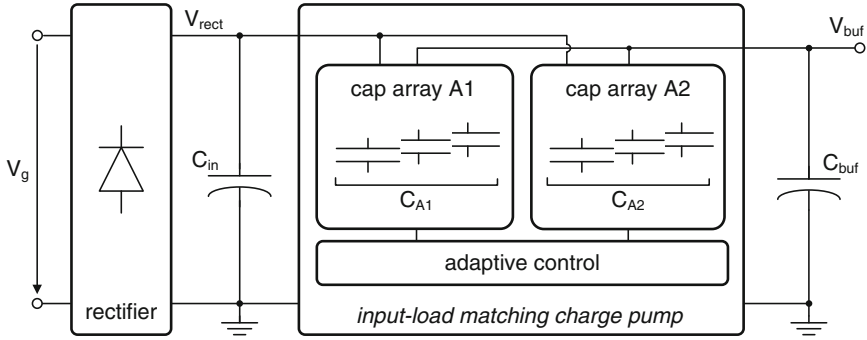


Fig. 2.18 Two out-of-phase toggled flying capacitor arrays are used for realizing the MPPT interface

loading of the transducer sampling of the actual open-circuit voltage $V_{g,oc}(t)$ is not possible anymore.

Altogether, the ILACP acts as the first converter of the two-stage power processing chain of Fig. 2.1, i.e. C_{buf} stores the harvested energy. Hence, both requirements can be achieved: fractional MPP harvesting with CFVT2, and controllable voltage conversion for not blocking the transducer current flow with high buffer voltages (for decoupling the input current flow from the buffer voltage).

Interface Blocks Altogether, three control units are necessary to stop charging at the voltage fraction V_{stop} , to determine the necessary voltage up-conversion ratio k_V , and finally to control the switch matrix for appropriate configuration of array switches. Thereby, adaptation of k_V is necessary either to deal with variable and non-sinusoidal input waveforms, or because of a fluctuant buffer voltage V_{buf} . The complete description is provided in Chap. 6.

Specifications Aspects Due to the limited area and capacitance possible at a fully-integrated solution total array capacitance of below 10 nF is possible only. As derived in Sect. 2.3.2.4, such a capacitance is close to $C_{in,min}$, which corresponds to transfer cycles (T_{chg}) as short as a few μs only. But it allows a fully-integrated interface suitable for highly integrated applications such as system-in-package (SiP) devices.

Besides these performance requirements, also the fluctuant supply voltage supply voltagevariability (V_{buf} is between sub-1 V and maximum CMOS rating $V_{DD,max}$) challenges the design of a beneficial system. Finally, for efficient operation a very limited power budget of only some tens of μW need to be considered. As a consequence, the control units can not deal with complex and fast clocked signal processing units, e.g. for charge control with a sufficient resolution of T_{chg} . The same is true for defining and updating V_{stop} . Hence, an event-driven comparator based approach is suggested for a low-power architecture with short response times at a low supply power level.

2.4.3 Adaptive Switched Inductor Capacitive Interface—SICI

The toggling approach of the ILACP means a lot of switching activity and costly speed requirements, as well as short but regularly repeated interruption of continuous power extraction. Therefore, a further implementation with an off-chip switched inductor is suggested. In conclusion, the SICI interface has the same functionality as the ILACP, i.e. it stores the harvested energy efficiently on C_{buf} while maintaining continuous FVT.

Interface Blocks As illustrated in Fig. 2.19, input capacitance C_{in} is permanently connected to the input (rectifier), and a load matching detector (LMD) generates the reference for the fractional MPP harvesting. Hence, the voltage conversion and POPoC window control is achieved with a switch-mode converter triggered by the LMD.

Specifications Aspects The idea is to have a C_{in} rather close to $C_{\text{in,max}}$, which is located off-chip like the inductor L_{tx} . Hence, C_{in} can harvest energy permanently, and switching activity will be reduced.

Using the LMD instead of the simple sampling mechanism (as suggested for the ILACP), causes a more complex detector method. Particularly in case of dynamic AC voltages it has to derive continuously an accurate voltage proportional to the optimal V_{stop} . In addition, due to the off-chip elements, the construction size is larger, and the switched inductor could be critical for certain EMI sensitive applications.

In summary, this approach gives the opportunities of tracking of AC and DC voltages, no toggle gaps are present, i.e. more continuous harvesting is possible, maximum power points are programmable by appropriate configuration of the MPPT detector (LMD), continuous instead of discrete adjustment of k_V is given, less switching activity is required, as well as a reduced power path design complexity. The chip implementation of this interface converter is shown in Chap. 8. The detector is separately discussed in Chap. 7.

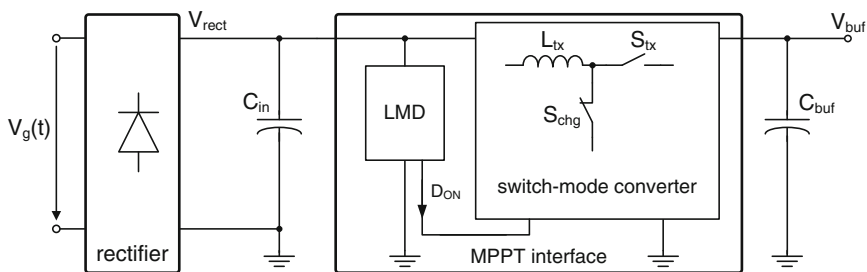


Fig. 2.19 The load matching detector (LMD) triggers the operation of the switch-mode voltage converter so as to track an power-optimal voltage on C_{in}

2.4.4 Stage 2—Application Voltage Converter

Since in most applications the ambient excitation is fluctuant, the output power which is already quite low is unstable as well. Thus, because MPPT interfaces can not control the actual buffer voltage V_{buf} , a large variation of voltage V_{buf} might appear. A severe obstacle of using such novel supply methods is that many modern integrated mixed-signal systems, e.g. autonomous sensor applications, still require a stable 3.3 V or 5 V supply [7]. That is, efficient voltage up-conversion with large voltage conversion ratios over a wide load range are necessary so as to supply various application modules with reliable and well defined voltage conditions.

Converter Blocks A basic schematic of a typical inductive boost converter is shown in Fig. 2.20. An analog control provides a pulse-width modulated (PWM) signal to a drive stage so as to bring the output voltage V_{out} to the intended value. Typically, the amplifier based analog PI controller defines a control voltage out of the difference between a feedback voltage V_{fb} and a fix reference voltage V_{ref} . Hence, an error amplifier tunes the control voltage V_{ctr} for adjusting the duty cycle of the pulse-width modulator. Since this is crucial for controlling the required output voltage V_{out} , the typically employed sawtooth generator and high-speed comparator are identified as critical at low supply voltages [14].

Specifications Aspects As the supply voltage will be non-constant and power consumption is critical, alternative solutions are preferred for achieving low-power operation. Thus, even though the loop bandwidth is not particularly high (e.g. few 10 kHz [7, 15, 16]), the PWM comparator faces challenging delay constraints (e.g. $t_{\text{d,min}}$ below some 10 ns). Circuit and system solutions are presented in Chap. 4.

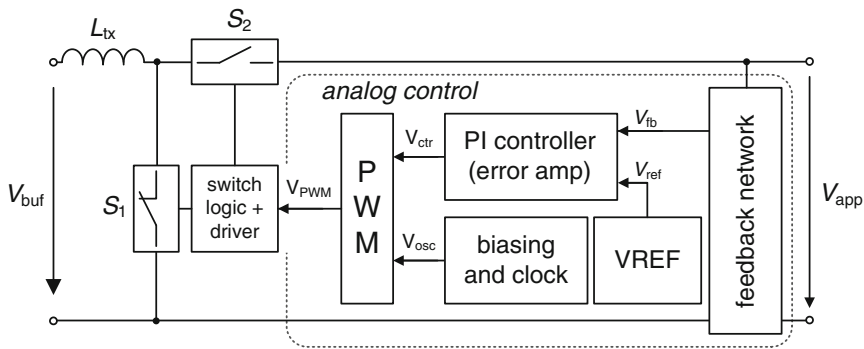


Fig. 2.20 Building blocks of a typical inductive switch-mode boost converter

2.5 Summary on Transducer Interface Requirements

This Chapter provided general concerns along the power-processing chain necessary for providing harvested energy to an application. Thereby, special findings regarding the employment of electromagnetic vibration transducers has been studied, and interface solution are derived.

Two-Stage Power Processing Chain As ambient μ EH sources provide intermittent and low-frequent input voltages and (non-sinusoidal) waveforms, a two stage power processing chain concept has been introduced in Sect. 2.1. While a first interface converter stores the harvested energy on a buffer (C_{buf}) while maintaining fractional MPP harvesting, the second converter takes the energy stored in C_{buf} and provides it to an application at a stabilized voltage level. Further power processing chain considerations reveal different efficiency definitions: harvesting efficiency, which includes the load matching effect, and device efficiency, which evaluates operation losses.

Optimized Transducer Loading In Sect. 2.2, primarily the optimal loading for MPP harvesting of small-scale electromagnetic vibration transducers is studied. As it turns out, both, continuous as well as averaged fractional voltage tracking allows a high degree of MPP harvesting, whereas the former is superior particularly for MPP tracking of non-sinusoidal waveforms.

Interfacing Concept In order to realize fractional voltage tracking, Sect. 2.3 introduces a method that approximates fractional voltage tracking by establishing a narrow voltage band in the vicinity of the optimal load point. This method allows a high efficient power extraction, while allowing low-power operation and low switching activity.

Circuit and System Design The implementation concepts presented in Sect. 2.4 need all to deal with the wide supply voltage range (V_{buf} is between sub-1 V and the maximum CMOS rating $V_{\text{DD,max}}$), and the very limited power budgets. Hence, the implementation of such concepts has particular requirements on analog circuit design. Most important is the development of appropriate structures and architectures, as well as innovative circuit design solutions, which can efficiently operate at the given operation conditions.

As harvesting is the focus, the second stage DC/DC converter for application supply control is not a main aspect of this book. Thus, rectification and MPP interfacing is focused. However, for ensuring that the complete two-stage power processing chain will be feasible within the considered supply range, the provided circuit designs in Chaps. 3 and 4 also address the basic building blocks necessary to assemble an output voltage converter.

References

1. S. Beeby, Energy harvesting network [Online] (2012), <http://eh-network.org/>
2. S. Cheng, N. Wang, D.P. Arnold, Modeling of magnetic vibrational energy harvesters using equivalent circuit representations. *J. Micromech. Microeng.* **17**, 2328–2335 (2007)
3. S. Roundy, P. Wright, J. Rabaey, *Energy Scavenging for Wireless Sensor Networks with Special Focus on Vibrations* (Kluwer Academic, Boston, 2003)
4. T. Sterken, K. Baert, R. Puers, S. Borghe, Power extraction from ambient vibration, in *Proceedings of Workshop on Semiconductor Sensors*, pp. 680–683 (2002)
5. D. Spreemann, B. Folkmer, Y. Manoli, Comparative study of electromagnetic coupling architectures for vibration energy harvesting devices, in *Proceedings of PowerMEMS 2008*, pp. 257–260 (2008)
6. D. Maurath, P. Becker, D. Spreemann, Y. Manoli, Efficient energy harvesting with electromagnetic energy transducers using active low-voltage rectification and maximum power point tracking. *IEEE J. Solid-State Circuits* **47**(6), 1369–1380 (2012)
7. D. Spreemann, Optimized design of resonant electromagnetic vibration energy harvesting devices, Ph.D. dissertation, University of Freiburg, 2011
8. P.D. Mitcheson, E.M. Yeatman, G.K. Rao, A.S. Holmes, T.C. Green, Energy harvesting from human and machine motion for wireless electronic devices. *Proc. IEEE* **96**(9), 1457–1486 (2008)
9. D. Spreemann, B. Folkmer, Y. Manoli, Realization of nonlinear springs with predefined characteristic for vibration transducer based on beam structures, in *Proceedings of PowerMEMS 2010*, pp. 371–374 (2010)
10. D. Spreemann and P. Becker, Energieautarke sensorik im kfz gespeist aus einem elektromagnetischen vibrationswandler, in *Proceedings of Internationales Forum Mechatronik* (2008)
11. E. Arroyo, A. Badel, Electromagnetic vibration energy harvesting device optimization by synchronous energy extraction. *Sens. Actuators A Phys.* **171**(2), 266–273 (2011)
12. P.D. Mitcheson, T.C. Green, E.M. Yeatman, Power processing circuits for electromagnetic, electro-static and piezoelectric inertial energy scavengers. *Microsyst. Technol.* **13**(7), 1629–1635 (2007)
13. Y. Tan, S. Panda, Optimized wind energy harvesting system using resistance emulator and active rectifier for wireless sensor nodes. *IEEE Trans. Power Electron.* **26**(1), 38–50 (2011)
14. D. Maurath, C. Peters, T. Hehn, N. Lotze, S.A. Mohamed, Y. Manoli, Energiesparende elektronik f selbstversorgende autarke systeme. *tm - Technisches Messen* **76**(12), 560–567 (2009)
15. S. Zhou, G.A. Rincon-Mora, A high efficiency, soft switching dc-dc converter with adaptive current-ripple control for portable applications. *IEEE Trans. Power Electron.* **53**(4), 319–323 (2006)
16. H.P. Forghani-Zadeh, G.A. Rincon-Mora, Low-power cmos ramp generator circuit for dc-dc converters. *J. Low Power Electron.* **2**(3), 437–441 (2006)

CMOS Circuits for Electromagnetic Vibration
Transducers

Interfaces for Ultra-Low Voltage Energy Harvesting

Maurath, D.; Manoli, Y.

2015, XXIII, 300 p. 155 illus., Hardcover

ISBN: 978-94-017-9271-4